


Article

Reduction of p-Nitrophenol with Modified Coal Fly Ash Supported by Palladium Catalysts

Hao Zhang, Kaicheng Zhou, Tao Ye, Huajun Xu, Man Xie, Pengfei Sun *  and Xiaoping Dong

Key Laboratory of Surface & Interface Science of Polymer Materials of Zhejiang Province, School of Chemistry and Chemical Engineering, Zhejiang Sci-Tech University, Hangzhou 310018, China

* Correspondence: sunpf@zju.edu.cn

Abstract: The compound p-Nitrophenol (p-NP) is widely recognized as a highly toxic nitro-aromatic substance that urgently requires emission control. Reducing p-NP to p-aminophenol (p-AP) not only decreases its toxicity and mineralization properties in nature but also provides a key raw material for the chemical and pharmaceutical industries. The study used coal fly ash (CFA) as a catalyst carrier for synthesizing the p-NP reduction catalyst. Using CFA as an alternative option not only reduces costs but also achieves the objective of treating waste with waste compared to utilizing commercial solid materials for synthesizing catalysts. By employing hydrochloric acid and sodium hydroxide pretreatment methods, the physicochemical properties of CFA are significantly improved, enhancing the dispersion of palladium (Pd) nanoparticles. The structural features of the prepared samples were characterized using various surface analysis techniques, and both intermittent and continuous modes were experimentally tested for the model catalytic reaction involving the sodium borohydride (NaBH₄)-mediated reduction of p-NP. The results demonstrate that CFA has potential in wastewater treatment.

Keywords: p-Nitrophenol; catalytic reduction; sodium borohydride; coal fly ash; palladium



Citation: Zhang, H.; Zhou, K.; Ye, T.; Xu, H.; Xie, M.; Sun, P.; Dong, X. Reduction of p-Nitrophenol with Modified Coal Fly Ash Supported by Palladium Catalysts. *Catalysts* **2024**, *14*, 600. <https://doi.org/10.3390/catal14090600>

Academic Editor: Adam F. Lee

Received: 30 July 2024

Revised: 20 August 2024

Accepted: 30 August 2024

Published: 6 September 2024



Copyright: © 2024 by the authors. Licensee MDPI, Basel, Switzerland. This article is an open access article distributed under the terms and conditions of the Creative Commons Attribution (CC BY) license (<https://creativecommons.org/licenses/by/4.0/>).

1. Introduction

The compound p-NP is widely recognized as a highly toxic nitro-aromatic substance, inflicting severe damage to the central nervous system, skin, kidneys, and liver in humans [1]. Furthermore, p-NP exhibits remarkable stability and solubility, making it extensively utilized in various industrial sectors such as rubber production, dye manufacturing, pharmaceutical development, and pesticide formulation. Consequently, p-NP has become ubiquitous in the environment [2]. Due to its pervasive presence and toxicity levels of concern, the United States Environmental Protection Agency (USEPA) has classified p-NP as a priority hazardous pollutant since 1979. As a result of this classification, strict regulations have been imposed on water sources to limit the concentration of p-NP to less than 10 ng L⁻¹ [3,4]. Considering the detrimental effects that nitrophenol poses on human health, it becomes imperative to degrade this compound into less harmful substances.

The current techniques employed for the degradation of p-NP encompass adsorption, photocatalysis, microbiological approaches, catalytic wet air oxidation, and nitro-reduction, among an array of other methodologies [5,6]. The adsorption method for p-NP removal relies on the physical interaction between the adsorbent and p-NP, however, it is time consuming, incomplete, and necessitates additional devices for collecting the adsorbate [7]; the photocatalytic degradation of p-NP necessitates expensive light devices; the microbiological method for p-NP degradation is inefficient and yields highly toxic intermediate products [8,9]; and the catalytic wet air oxidation for p-NP degradation requires prolonged periods of high temperature and pressure to effectively eliminate p-NP [10]. In contrast, the reduction method is commonly used because of its obvious advantages, such as mild reaction conditions, simple reaction processing, and environmental friendliness [11–14].

The reduced product, p-aminophenol (p-AP), is both less toxic and easier to mineralize, and is also a key raw material for the production of drugs such as paracetamol and antomomycin [15]. Therefore, the selective reduction of p-NP to p-AP reduces not only environmental pollution but also creates economic value.

In recent years, noble metal nanoparticles have garnered considerable attention in the realm of multiphase catalysis, showcasing exceptional catalytic performance in numerous reactions owing to their expansive specific surface area and robust catalytic activity [16]. Among a wide array of precious metals, Pd nanoparticles and Pd-based complexes are frequently employed for catalytic hydrogenation due to their remarkable reduction capabilities [17]. Nonetheless, Pd nanoparticles possess an exceedingly high surface energy and are susceptible to agglomeration, which can significantly diminish their catalytic activity; moreover, homogeneous Pd catalysts prove arduous to separate and recover upon the completion of the catalytic reaction [18,19].

In order to tackle this predicament, researchers have augmented the catalytic prowess of Pd nanoparticles by embellishing and fortifying metallic Pd nanoparticles employing an array of solid materials such as graphene [20], silica [21], zeolite [22], metal–organic frameworks (MOFs) [23], covalent organic frameworks (COFs) [24], etc.

CFA is the main solid waste discharged from coal-fired power plants and mainly consists of unburned carbon, metal oxides, and other inorganic materials [25]. In recent years, due to the rapid development of the industry, the amount of CFA discharged has increased greatly, which will pollute the air and natural waters and affect the normal life of human beings [26]. To this end, a multitude of researchers have embarked on endeavors to metamorphose CFA into materials of elevated value. Currently, CFA has found utility in the fabrication of clay bricks, cement, agricultural fertilizers, and other commodities [27]. Due to the exceptional thermal stability of CFA, it is also employed as an adsorption catalytic material. Furthermore, the physicochemical properties of CFA can be significantly enhanced through various common modifications such as mechanical milling [28], acid modification [29], alkali modification [30], salt modification [31], and so forth. Wang et al. employed sulfuric acid treatment on CFA to augment its specific surface area, thereby enhancing the adsorption efficiency of ammonia in waste gas. The results of the study showed that the adsorption performance of acid-modified CFA increased by 427% compared to untreated CFA [32]. Niladri Maity et al., used CFA as a carrier loaded with Pd–Ag bimetallic for p-NP reduction, and the reduction performance was significantly enhanced by optimizing the metal ratio [33]. In addition, because the ratio of SiO₂ and Al₂O₃ in CFA is 60~80%, CFA is often used as a silica–aluminum source for the synthesis of zeolites. The results show that the 4A zeolite and ZSM-5 zeolite synthesized from CFA have good adsorption separation effects [34–36].

The utilization of commercial solid materials for synthesizing catalysts in p-NP degradation will inevitably escalate the expenses associated with industrial applications. However, employing CFA can be a more judicious alternative that not only curtails costs but also accomplishes the objective of treating waste with waste. Herein, CFA was modified using hydrochloric acid and sodium hydroxide, resulting in the release of amorphous sodium silicate and sodium aluminate from the surface of CFA. This structural change on the CFA surface facilitated the immobilization of Pd nanoparticles. Various surface analysis techniques were employed to characterize the prepared CFA samples, and different reaction parameters were also adjusted to evaluate their catalytic reduction performance. The results demonstrated significant p-NP reduction performance and promising potential for industrial applications.

2. Results and Discussion

2.1. Surface Characteristics of Different Coal Fly Ash Samples

Figure 1 demonstrates the morphological and structural features of CFA, CFA(H) (the CFA with HCl heat treatment), and CFA(H+Na) (the CFA(H) with NaOH heat treatment) characterized by SEM at different optical magnifications. As shown by electron microscopy,

the pristine CFA exhibits typical spherical aluminosilicate features [37]. Compared with CFA, CFA(H) also inherited this spherical morphology. However, the specific surface area (S_{BET}) and the total pore volume (V_{total}) of CFA(H) exhibited a slight increase compared to the untreated CFA, as detailed in Table 1. This enhancement can be ascribed to the acid modification process, which effectively removed surface impurities and alkali metal salts, thereby activating the pore structures and enhancing the material's overall surface area and pore volume [25].

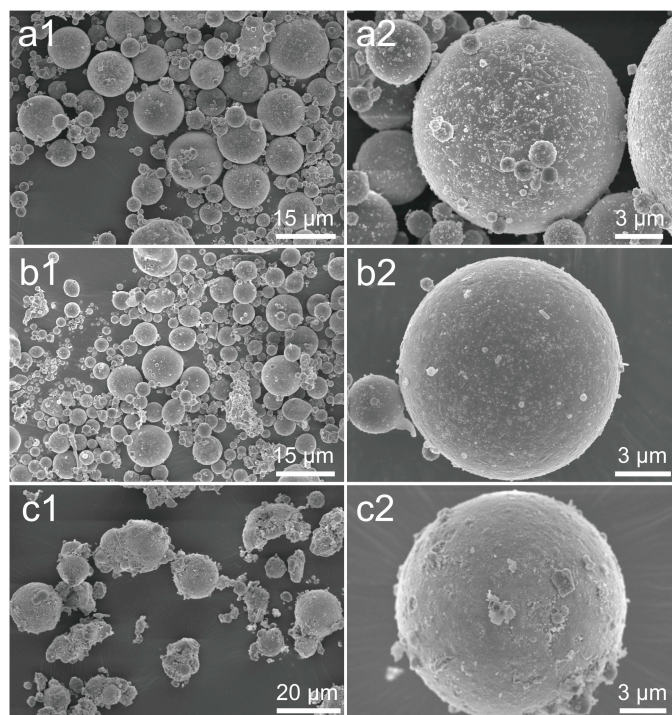


Figure 1. SEM images of CFA (a1,a2), CFA(H) (b1,b2), and CFA(H+Na) (c1,c2).

Table 1. Pore parameters and elemental contents of different CFA samples.

Samples	S_{BET} (m^2/g)	V_{total} (cm^3/g)	Pore Size (nm)	ICP Analysis (10^{-2} g/g)					
				Si	Al	Ca	Fe	Mg	Pd
CFA	1.47	0.0047	8.14	19.04	16.03	3.99	3.77	0.74	/
CFA(H)	11.37	0.0083	9.72	15.71	15.15	1.03	1.32	0.21	/
CFA(H+Na)	66.61	0.1443	10.68	9.75	12.36	0.67	0.98	0.13	/
Pd-CFA(H+Na)	67.35	0.1022	9.65	9.62	12.16	0.81	0.85	0.08	1.23

The ICP results in Figure 2 also prove that the contents of Mg ions, Ca ions, and Fe ions on the surface of pristine CFA were significantly reduced under the effect of acid treatment. After alkali modification, the surface of CFA(H+Na) became even rougher and large cracks appeared, which was mainly due to the surface mullite and quartz that dissolved like sodium silicate and sodium aluminates [38,39]. This treatment significantly expanded the specific surface area and enhanced the pore structure of CFA(H). The ICP results also showed that the Si and Al elements were significantly reduced after alkali treatment.

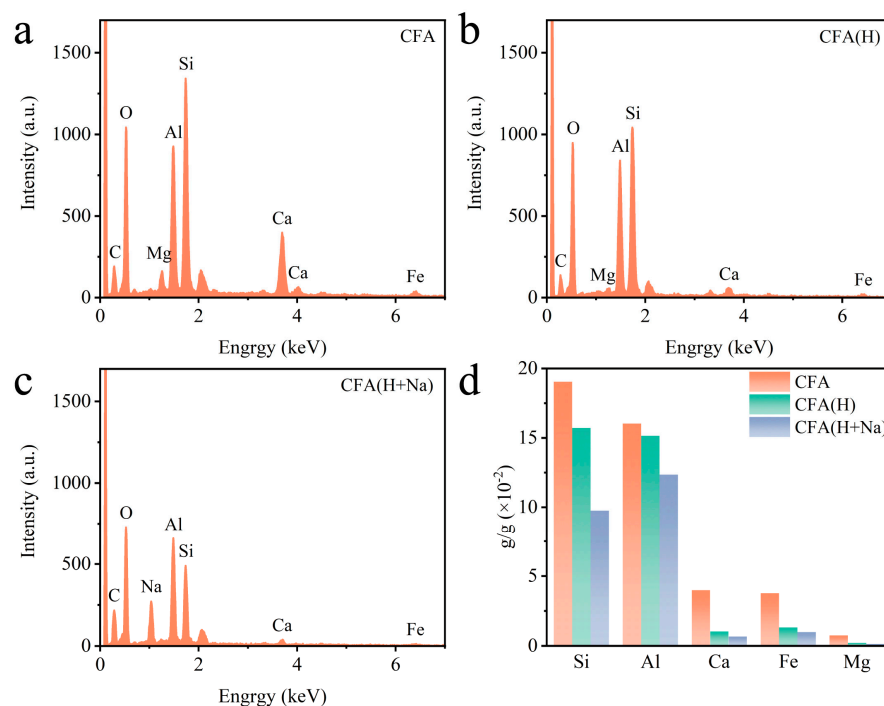


Figure 2. EDS analyses of (a) CFA, (b) CFA(H), and (c) CFA(H+Na); (d) ICP analyses of CFA, CFA(H), and CFA(H+Na).

The XRD spectra of different CFA samples are shown in Figure 3, where the characteristic peaks at $2\theta = 16.4^\circ, 26.0^\circ, 26.3^\circ, 31.0^\circ, 33.2^\circ, 35.3^\circ, 40.9^\circ, 42.6^\circ,$ and 60.7° belong to mullite, and the characteristic peaks at $2\theta = 20.9^\circ, 26.6^\circ, 36.5^\circ, 50.1^\circ,$ and 60.0° belong to quartz [40]. In addition, the presence of distinct diffuse packet peaks between $2\theta = 15^\circ$ and 30° suggest that CFA contains a significant amount of amorphous glassy phase material [41,42]. After acid modification, the XRD spectra of CFA(H) did not change significantly compared with the original CFA. After further alkali modification, the diffuse packet peaks between $2\theta = 15^\circ$ and 30° disappeared markedly, indicating that the amorphous glassy phase material of the CFA had been dissolved by sodium hydroxide. The crystallinity of the Pd-CFA(H+Na) sample did not change significantly after Pd nanoparticle loading, and no characteristic peaks of Pd were found in the XRD pattern of this sample. Figure S1 shows the XRD spectra of Pd-CFA(H+Na) with different Pd loadings, and no characteristic peaks of Pd were detected for all Pd-CFA(H+Na) samples, which is attributed to the low content of Pd loading with superior dispersion.

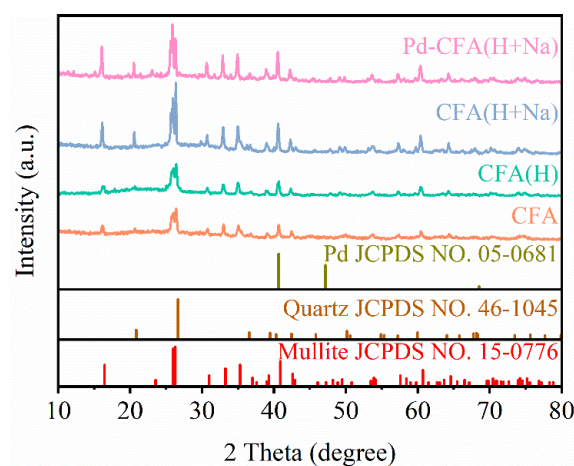


Figure 3. XRD spectra of CFA, CFA(H), CFA(H+Na), and 1.25 wt% Pd-CFA(H+Na).

The EDS mapping analysis of Pd-CFA(H+Na) was carried out (see Figure 4) in order to observe the distribution of Pd nanoparticles on CFA(H+Na), which exhibit that the Pd nanoparticles that were well dispersed over CFA(H+Na) consisted of other elements (Figure 5). The ICP results indicated that the mass fraction of Pd in the catalysts prepared by the impregnation reduction method was about 1.23 wt%, aligning with the theoretical value and confirming the successful loading of Pd nanoparticles onto CFA(H+Na).

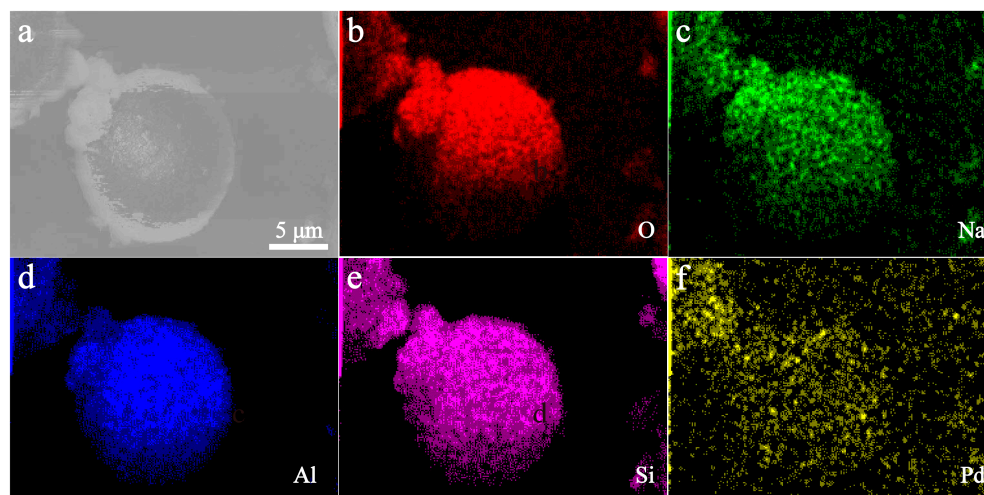


Figure 4. EDS mapping of 1.25 wt% Pd-CFA(H+Na). Catalysts: electron mapping of (a) 1.25%-Pd-CFA(H+Na); (b) O; (c) Na; (d) Al; (e) Si; (f) Pd.

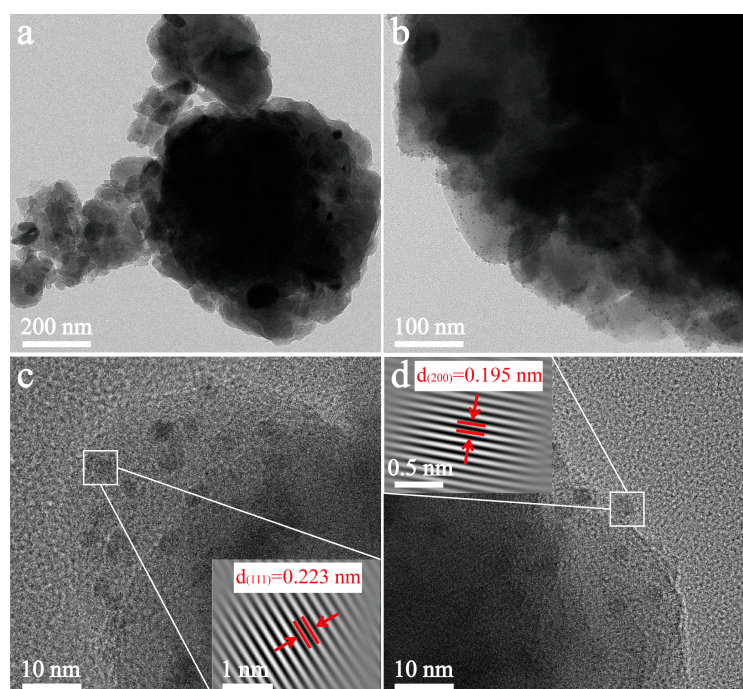


Figure 5. TEM image of 1.25 wt% Pd-CFA (H+Na). Catalysts: (a,b) TEM; (c,d) HRTEM.

The TEM and HRTEM images of Pd-CFA(H+Na) are shown in Figure 5 where the black dots are highly dispersed Pd NPs with uniform size, and no agglomerated state was found. The exposed lattice stripes of Pd nanoparticles with a lattice stripe spacing of 0.223 nm and 0.195 nm belonged to the Pd (111) crystallographic plane and the Pd (200) crystallographic plane, respectively [43,44].

An XPS analysis of Pd-CFA(H+Na) was also carried out. Figure 6a shows the full XPS spectrum of Pd-CFA(H+Na), where the presence of carbon, oxygen, and Pd elements on the surface of the catalyst was observed. Figure 6b shows the Pd 3d pattern of the Pd-CFA(H+Na) sample, which can be fitted to four peaks. The peaks at 335.4, 336.2, 340.7, and 341.5 eV correspond to Pd⁰3d_{5/2}, Pd²⁺3d_{5/2}, Pd⁰3d_{3/2}, and Pd²⁺3d_{3/2}, respectively [45,46]. Analyzed by the convolutions of the peak areas, the contents of Pd⁰ and Pd²⁺ can be calculated as 76.34% and 23.66%, indicating that the loaded Pd nanoparticles are mainly present as Pd⁰.

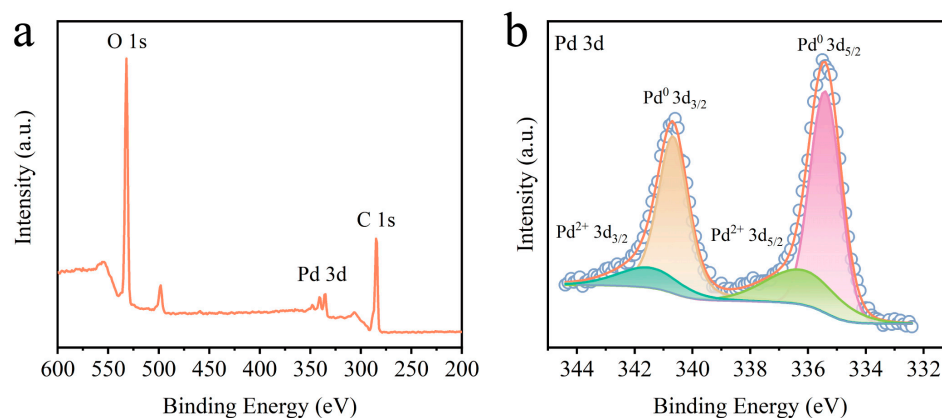


Figure 6. (a) XPS total spectrum of Pd-CFA(H+Na); (b) XPS spectrum of Pd 3d.

2.2. Reduction Performance of *p*-Nitrophenol

The catalytic performance of Pd-CFA(H+Na) was assessed by utilizing NaBH₄ to reduce *p*-NP to *p*-AP. In Figure 7a, a distinct absorption peak at 317 nm can be observed for the aqueous solution of *p*-NP. Upon the addition of NaBH₄, the absorption peak shifted to 400 nm due to the acid–base reaction between *p*-NP and NaBH₄, resulting in the formation of a *p*-NP anion [47]. The ratio of the concentration of *p*-NP at time *t* to the initial concentration is estimated from the Beer–Lambert law.

$$\ln(A_t/A_0) = \ln(C_t/C_0) = -k_{\text{obs-p-NP}}(t - t_0), \quad (1)$$

(C_t and A_t are the concentration of *p*-NP at moment *t* and the absorbance value at λ = 400 nm; C₀ and A₀ are the initial concentration and absorbance value of *p*-NP).

The freshly prepared NaBH₄ solution did not reduce *p*-NP in the absence of catalyst presence (Figure 7b). The changes in the characteristic peaks of 1.25 wt% Pd-CFA(H+Na) in the reduction of *p*-NP under the condition of NaBH₄ as the reducing agent are shown in Figure 7c. As the reaction proceeds, the absorption peak of *p*-NP at 400 nm gradually decreases, the absorption peak of the reduced product, *p*-AP, at 298 nm gradually enhances, the absorption peak of *p*-NP completely disappears after 5 min, and the color of the solution changes from bright yellow to colorless (see Figure S2), indicating that *p*-NP is completely reduced [48]. Based on the good linear relationship between ln(A_t/A₀) and reaction time (Figure 7d), the apparent rate constant (*k*) for the *p*-NP reduction reaction of Pd-CFA(H+Na) was calculated to be 0.95 min^{−1} (R² = 0.99), which exhibits preferable *p*-NP reduction activity compared to recently reported noble metal-based materials (see Table 2).

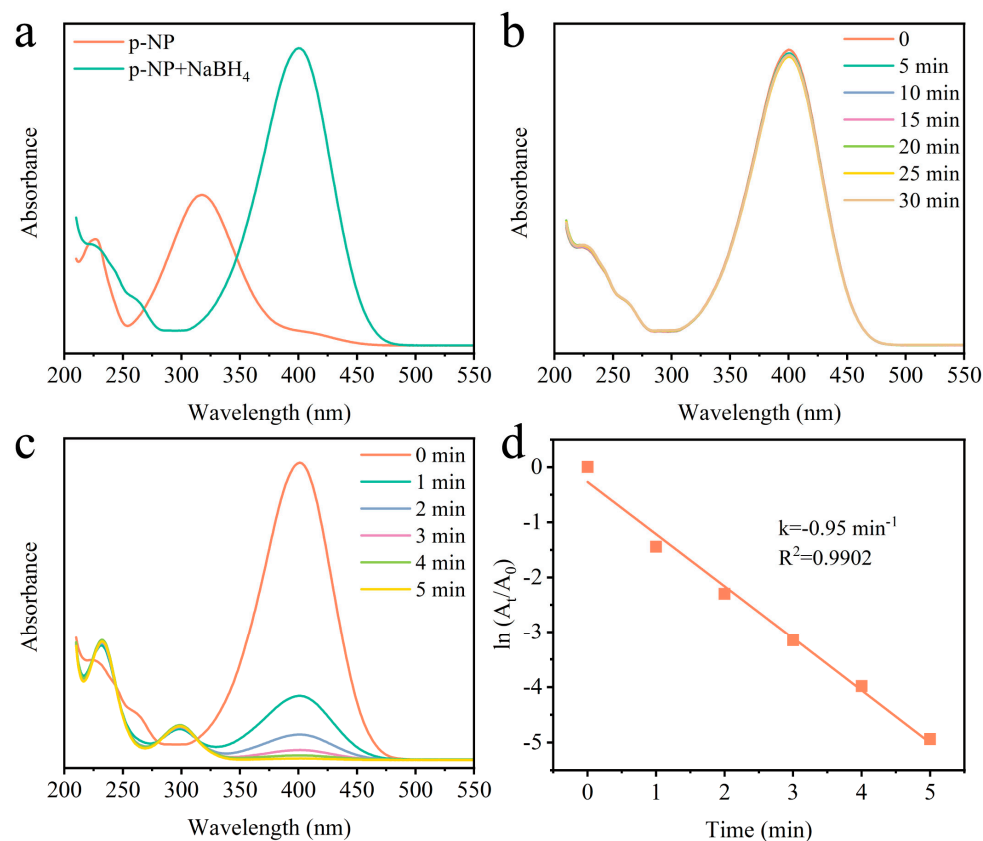
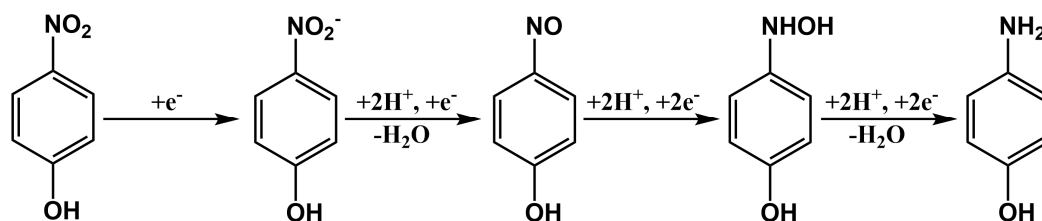


Figure 7. (a) UV–visible absorption spectra of p-NP solution before and after addition of NaBH₄; (b) UV–vis absorption spectra of p-NP+NaBH₄ in the absence of Pd-CFA(H+Na) within 30 min; (c) UV–visible absorption spectra of the catalytic reaction performance of p-NP+NaBH₄+Pd-CFA(H+Na) at different time intervals within 5 min; and (d) rate constant of 1.25 wt% Pd-CFA(H+Na) reduction of p-NP.

Table 2. Comparison of the performance of metal catalysts for the reduction of p-NP in the presence of NaBH₄.

Catalysts	C _{p-NP} (mM)	C _{NaBH₄} (mM)	C _{cat} (g/L)	k (min ⁻¹)	Ref.
Fe ₃ O ₄ @COF-Au	1.0	440	0.33	0.22	[49]
Pd@MOPOH	0.1	10	0.16	0.65	[50]
Ag/CA2.0	0.14	28.8	1	0.34	[51]
Cu/CMC	0.13	50	1.67	0.21	[52]
Cu/Cs@CMC	0.13	50	1.67	0.38	[52]
ZnO-SiO ₂ -Ag	0.1	7.5	2.5	0.26	[53]
FA-Pd-Ag	0.01	1	0.2	0.72	[54]
Au@g-C ₃ N ₄	0.2	7	1	0.9	[55]
Pd-CFA(H+Na)	0.8	40	1	0.95	This work

In contrast, CFA(H+Na) showed almost no reduction performance (Figure S3). Therefore, the reduction of p-NP can be catalyzed by Pd-CFA(H+Na) only when Pd serves as the active center, providing the catalytic reaction site. The possible mechanism for the reduction of p-NP by Pd-CFA(H+Na) is exhibited in Scheme 1. Firstly, p-NP is converted to p-NP ions due to the increase in solution pH by the addition of NaBH₄. Then, the active hydrogen from [BH₄]⁻ will be transferred to the metal nanoparticles to generate the metal hydride. Concurrently, the catalyst continues to adsorb the active hydrogen from [BH₄]⁻ to reduce p-NP in the solution to nitrosophenol and p hydroxyphenol, and finally, to p-AP [56,57].



Scheme 1. Reaction pathway for catalyst reduction of p-NP to p-AP.

2.3. Reaction Parameter Influence

The impact of Pd loading on the catalytic performance of the catalysts was investigated and shown in Figure 8a, unveiling the determination of an optimal loading. The catalytic activity exhibited a gradual enhancement with increased loading, reaching its pinnacle at 1.25 wt%, which achieved a complete reduction of p-NP within a mere 5 min. However, further increments in Pd loading will lead to a subsequent decline in catalytic activity due to the potential agglomeration of Pd nanoparticles on the catalyst surface [15]. The effect of p-NP concentration on the performance of the catalyst for the reduction of p-NP was also investigated. Figure 8b illustrates the plot of A_t/A_0 as a function of reaction time. Based on the experimental findings, it is evident that the reduction efficiency remained relatively constant when the concentration was increased from 0.1 mM to 0.8 mM; however, it decreased upon further increasing the concentration to 1.6 mM due to the excessive adsorption of p-NP onto the Pd-CFA(H+Na) surface. This excess p-NP competed for limited adsorption sites, thereby impeding electron transfer from $[BH_4]^-$ to p-NP [58]. The catalyst dosing during the reaction process was also evaluated by varying the dosage of Pd-CFA(H+Na) from 0.25 g/L to 2 g/L (Figure 8c). Undoubtedly, the rate of reduction experiments gradually escalated with increasing catalyst dose, attributed to the heightened activity sites of the catalyst for rapid reduction of a limited quantity of p-NP.

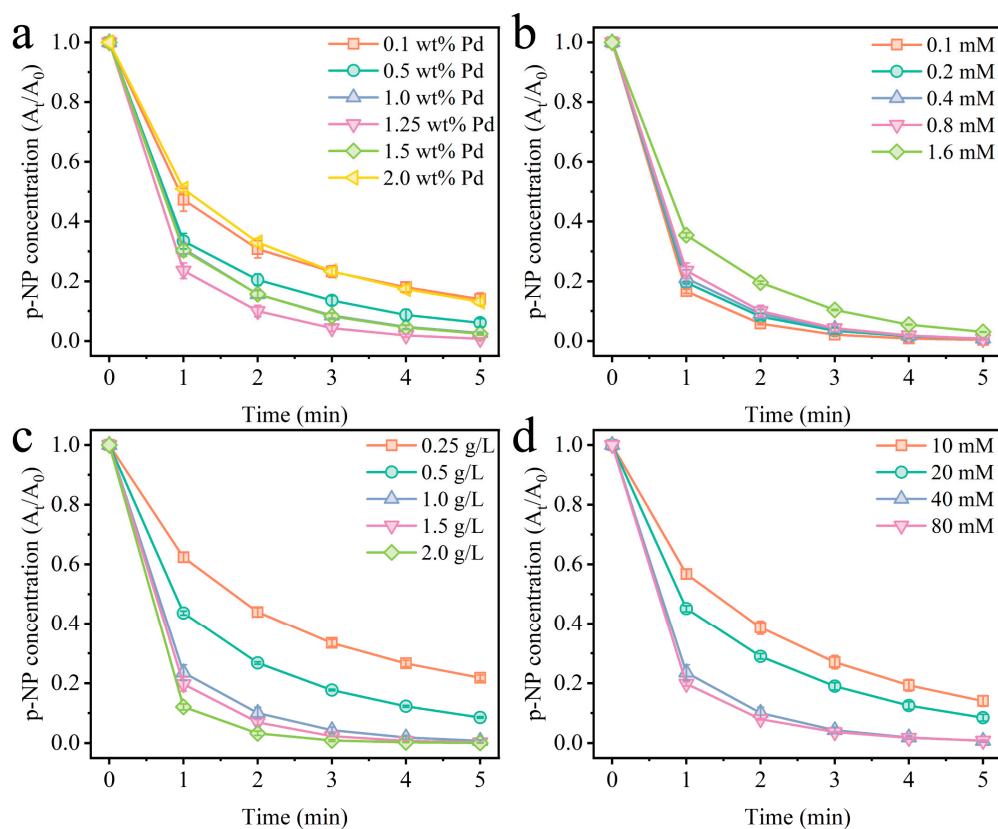


Figure 8. Effect of different reaction conditions on the performance of reduced p-NP: (a) Pd loading; (b) p-NP concentration; (c) catalyst injection; and (d) $NaBH_4$ concentration.

In this experiment, NaBH_4 serves as the hydrogen donor for the catalytic reaction, thus emphasizing the significance of varying NaBH_4 concentrations on the performance of p-NP reduction. Figure 8d illustrates a clear trend where an elevated NaBH_4 concentration leads to an enhanced catalytic reduction efficiency. This phenomenon can be attributed to the fact that higher levels of NaBH_4 result in an increased abundance of NaBH_4 ions, which in turn provide more hydrogen for the conversion of p-NP into p-AP [59]. However, it is noteworthy that beyond a certain point (specifically when increasing from 40 mM to 80 mM), further increments in NaBH_4 concentration do not yield any additional improvements in reaction efficiency or rate. This observation suggests that under these reaction conditions, there exists a saturation point regarding $[\text{BH}_4]^-$ ion availability and consequently, the excessive addition of NaBH_4 becomes impractical due to cost considerations.

2.4. Stability Test of Catalyst

The durability and stable utilization of the catalyst are pivotal in practical applications. Following the catalytic reaction, the catalyst was separated and utilized for subsequent catalytic experiments. Figure 9a depicts that the reduction performance of the catalyst exhibited a decline after undergoing five cycles of experimentation, potentially attributed to a slight loss in catalyst quality during pretreatment at different reaction intervals. Figure 9b compares the XRD patterns of Pd-CFA(H+Na) before and after five cycles of experimentation, revealing no significant alteration in the structure of the catalyst, thereby indicating its exceptional structural stability.

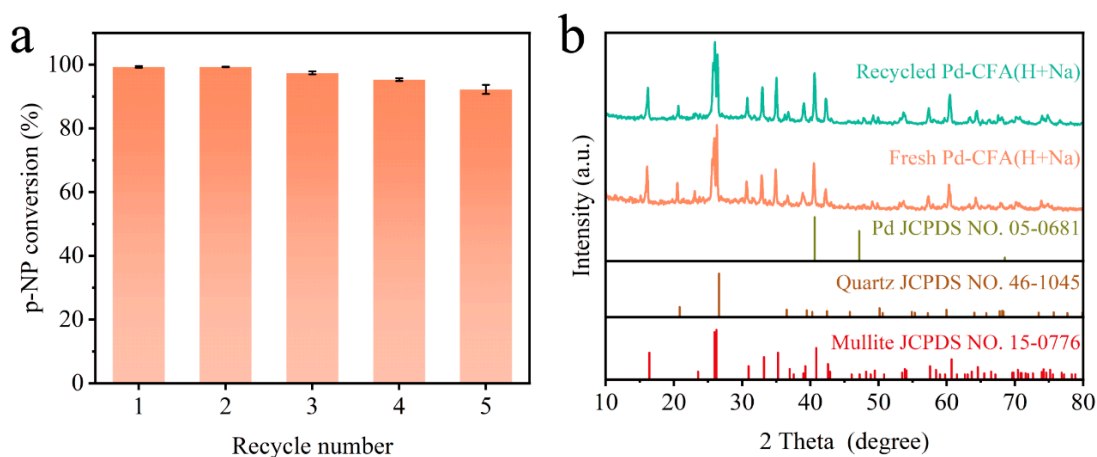


Figure 9. (a) Cycling performance test of reduced p-NP; (b) the XRD plots of Pd-CFA(H+Na).

2.5. Continuous Reaction Process

An investigation of the continuous reaction process was conducted to assess the practical applicability of the catalyst in terms of its p-NP reduction performance. As shown in Figure 10, Pd-CFA(H+Na) was immobilized in the fixed-bed reactor and then a mixture of p-NP and NaBH_4 was fed into the reactor via a peristaltic pump. The reaction solution was received through a beaker and the concentration of p-NP and p-AP was analyzed with UV spectrophotometry.

As shown in Figure 11a, when the flow rate was set to 1 mL/min and the concentration of p-NP was 0.8 mM, the UV-visible absorption peak of p-NP at 400 nm disappeared and a new peak appeared at 298 nm after passing through the reactor in the mixed solution, indicating the complete reduction of p-NP and the generation of the reduction product p-AP. The experimental results in Figure 11b are utilized to assess the stability of the catalyst. The continuous conversion of p-NP to p-AP (conversion rate exceeding 97%) can be sustained for over three hours (at a flow rate of 1 mL/min) and initiates a gradual decline in the subsequent two hours, nevertheless, maintaining a conversion rate above 90%. The incomplete desorption of a small portion of the reduction product p-AP may

potentially account for this phenomenon as it obstructs the interaction between the active site and p-NP [60].

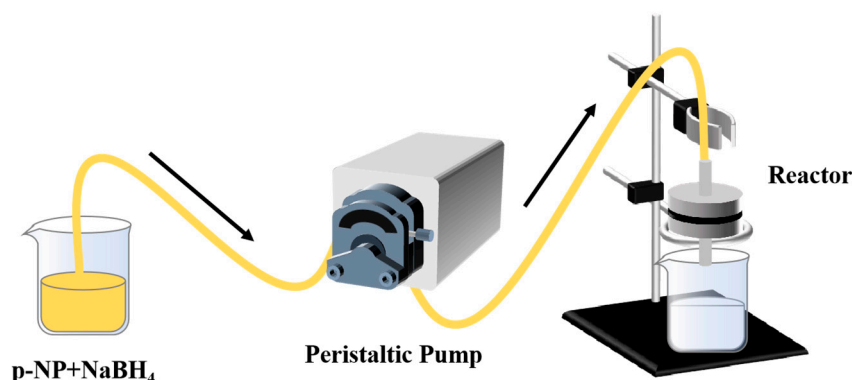


Figure 10. Schematic of the continuous flow filtration experiment in the fixed-bed reactor.

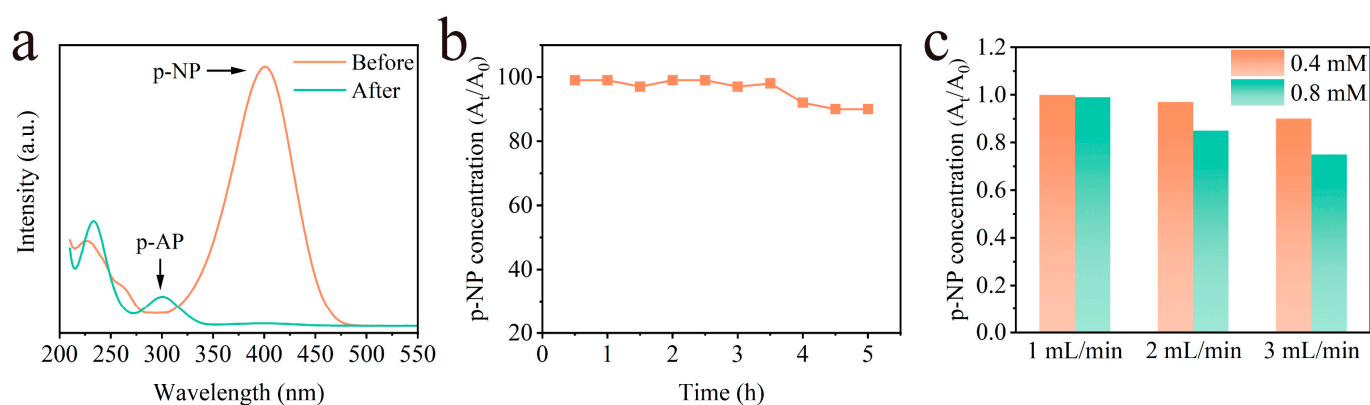


Figure 11. (a) UV–visible spectra of reactant solutions before and after flowing through the reactor; (b) durability test for the catalytic reduction of p-NP in the reactor (1 mL/min); (c) effect of different flow rates at different concentrations on the reduction performance of p-NP.

The impact of varying flow rates on the reduction experiments was also examined, and the experimental results are showcased in Figure 11c. It can be observed that as the flow rate increases from 1 mL/min to 3 mL/min, there is a decrease in the conversion of p-NP to p-AP. This decline is primarily attributed to the reduced reaction residence time in the fixed bed caused by an increase in flow rate, consequently diminishing catalytic performance [61]. However, this phenomenon can be mitigated by reducing the concentration of the p-NP solution from 0.8 mM to 0.4 mM. The rapid catalytic reduction of p-NP using a fixed-reactor system reveals the potential practical application of this system.

3. Materials and Methods

3.1. Materials

The CFA was sourced from the Zhoushan Power Plant of China’s National Energy Group. The chemicals used in this study, which were concentrated hydrochloric acid (HCl, AR), concentrated sulfuric acid (H₂SO₄, AR), and acetone (C₃H₆O, AR), were purchased from Shuanglin Chemical Science and Technology Co., Ltd. (Huzhou, China). p-nitrophenol (p-NP > 99.5%), NaBH₄ (AR), and sodium tetrachloropalladate (Na₂PdCl₄, 98%) were purchased from Aladdin Chemical Technology Co., Ltd. (Shanghai, China). The deionized water was purified by Millipore’s Mill-Q system (Billerica, MA, USA), and the resistivity was >18.2 MΩ cm^{−1}.

3.2. Synthesis

The modification methods of CFA were as follows: 30 g of CFA screened through a 100-mesh filter ($<150\ \mu\text{m}$) was stirred with 300 mL of 1.2 mol/L HCl solution for 2 h at $85\ ^\circ\text{C}$. After stirring, it was separated by cooling and filtration; the filtrate was then rinsed with deionized water until the pH of the filtrate was neutral. After that, it was dried at $60\ ^\circ\text{C}$ overnight. The prepared catalysts were labelled for CFA(H).

Acid-modified CFA 30 g and 150 mL of 5 mol/L NaOH solution were mixed well and heated in a sealed oven at $100\ ^\circ\text{C}$ for 24 h. After the reaction, the filtrate was then rinsed with deionized water and ethanol until the pH of the filtrate was neutral, and dried at $60\ ^\circ\text{C}$ overnight. The prepared catalysts were labelled for CFA(H+Na).

The catalysts were prepared by an impregnation reduction method [62,63]: 1 g of CFA(H+Na) was dispersed in 15 mL of deionized water, mechanically stirred for 10 min, Na_2PdCl_4 (3.5 mL, 0.034 mol/L) solution was added, Na_2PdCl_4 solution was stirred with CFA(H+Na) suspension at room temperature and stirred for 0.5 h, then, the freshly configured NaBH_4 solution (0.05 mol/L, 5.0 mL) was added, and stirring continued at room temperature for 1 h. The catalyst was washed with deionized water and acetone by centrifugation and dried in a vacuum oven at $60\ ^\circ\text{C}$ for 2 h. The catalyst obtained was named 1.25 wt% Pd-CFA(H+Na).

3.3. Characterization

The structural information of different coal fly ash samples was measured by X-ray powder diffraction (XRD, Haoyuan DX-2700, Dandong, China) using Cu-targeted $\text{K}\alpha$ -ray radiation. The microstructures of different CFA samples were observed by using a scanning electron microscope (SEM, Hitachi SU-8100, Tokyo, Japan) equipped with an energy dispersive X-ray spectrometer (EDS) and a transmission electron microscope (TEM, JEM 2100, Tokyo, Japan). The nitrogen adsorption–desorption isotherms were detected by an ASAP 2020 analyzer (Micromeritics, Norcross, GA, USA). The inductively coupled plasma emission spectroscopy (ICP-OES) was measured using an iCAP PRO XP ICP-OES emission spectrometer (Thermo, Waltham, MA, USA). The specific surface area and pore size distribution of different CFA samples were determined using Brunauer-Emmet-Teller (BET) and Barrett-Joyner-Halenda (BJH). The samples were degassed at $300\ ^\circ\text{C}$ for 4 h before actual measurements. The total pore volume was calculated using the single-point method at a relative pressure (P/P_0) of 0.99. The elemental composition and chemical environment of the CFA samples were analyzed with X-ray photoelectron spectroscopy (XPS, Kratos AXIS Ultra DLD, Shimadzu, Kyoto, Japan).

3.4. Performance

The catalyst activity was evaluated using the ability of the catalyst to reduce p-NP in both batch and fixed-bed reactors; all experiments were carried out at a room temperature of $25\ ^\circ\text{C}$.

In the batch mode, 100 mg of Pd-CFA(H+Na) was dispersed into an aqueous solution of p-NP (0.8 mM, 100 mL) containing 0.04 M NaBH_4 for the reduction reaction. At the given time interval, 3 mL of reaction solution was collected and the experiment lasted for 5 min; the solution was filtered through a $0.22\ \mu\text{m}$ inorganic filter membrane to remove solids, and then diluted with deionized water. The filtered and diluted solutions were analyzed for changes in p-NP and p-AP concentrations with a UV spectrophotometer (UV-Vis, UV-2600, Shimadzu, Kyoto, Japan) detecting and recording the absorbance values of the reaction solutions at 400 nm and 298 nm. All experimental data were averaged over three replicates.

In the fixed-bed mode, 100 mg of Pd-CFA(H+Na) was immobilized in a catalytic reactor and different concentrations of p-NP were mixed with freshly prepared 0.04 M NaBH_4 , which was catalyzed by Pd nanoparticles; the reaction was carried out by a peristaltic pump at a certain flow rate through the reactor, and the solution flowing through Pd-CFA(H+Na) at 30 min was collected and diluted with deionized water; the p-NP and p-AP

concentrations in the solution were measured with UV spectrophotometer concentrations to achieve continuous dynamic catalysis.

4. Conclusions

Herein, CFA-based catalysts loaded with modified CFA as the carrier and Pd⁰ as the active phase were synthesized. The structural characterization of the CFA samples before and after modification was conducted using XRD, FESEM, TEM, ICP, and N₂ adsorption-desorption techniques. After acid–base modification, the specific surface area of CFA increased significantly from 1.47 m²/g to 66.61 m²/g. Furthermore, loading Pd greatly enhanced the reduction performance of p-NP. The catalytic deoxidizing reaction over the Pd-CFA(H+Na) catalyst exhibited exceptional conversion of p-NP to p-AP in both batch and fixed-bed reactions. This work demonstrates that CFA can be effectively transformed into an industrially valuable catalytic material through resource reuse.

Supplementary Materials: The following supporting information can be downloaded at <https://www.mdpi.com/article/10.3390/catal14090600/s1>: Figure S1: The XRD spectra of CFA with different Pd loadings; Figure S2: Left p-NP; middle p-NP added to NaBH₄ right after addition of catalyst reaction; and Figure S3: The comparison of the performance of different CFA samples for the reduction of p-NP.

Author Contributions: Conceptualization, H.Z. and K.Z.; methodology, H.Z. and K.Z.; validation, H.Z., K.Z. and T.Y.; investigation, H.Z.; writing—original draft preparation, H.X. and M.X.; writing—review and editing, X.D. and P.S.; supervision, X.D.; funding acquisition, P.S. All authors have read and agreed to the published version of the manuscript.

Funding: This research was financially supported by the Zhejiang Provincial Natural Science Foundation of China (LTGS24B070003).

Data Availability Statement: Data are contained within the article.

Conflicts of Interest: The authors declare no conflicts of interest.

References

1. Ghanbari, N.; Hoseini, S.J.; Bahrami, M. Ultrasonic assisted synthesis of palladium-nickel/iron oxide core-shell nanoalloys as effective catalyst for Suzuki-Miyaura and p-nitrophenol reduction reactions. *Ultrason. Sonochem.* **2017**, *39*, 467–477. [[CrossRef](#)] [[PubMed](#)]
2. Fan, P.; Zhang, X.; Deng, H.; Guan, X. Enhanced reduction of p-nitrophenol by zerovalent iron modified with carbon quantum dots. *Appl. Catal. B Environ.* **2021**, *285*, 119829. [[CrossRef](#)]
3. Tan, X.; Qin, J.; Li, Y.; Zeng, Y.; Zheng, G.; Feng, F.; Li, H. Self-supporting hierarchical PdCu aerogels for enhanced catalytic reduction of 4-nitrophenol. *J. Hazard. Mater.* **2020**, *397*, 122786. [[CrossRef](#)]
4. Bae, S.; Gim, S.; Kim, H.; Hanna, K. Effect of NaBH₄ on properties of nanoscale zero-valent iron and its catalytic activity for reduction of p-nitrophenol. *Appl. Catal. B-Environ.* **2016**, *182*, 541–549. [[CrossRef](#)]
5. Din, M.I.; Khalid, R.; Hussain, Z.; Hussain, T.; Mujahid, A.; Najeeb, J.; Izhar, F. Nanocatalytic Assemblies for Catalytic Reduction of Nitrophenols: A Critical Review. *Crit. Rev. Anal. Chem.* **2020**, *50*, 322–338. [[CrossRef](#)] [[PubMed](#)]
6. Liu, Y.; Liu, Y.; Xu, Y.; He, Q.; Yin, R.; Sun, P.; Dong, X. Phenanthroline bridging graphitic carbon nitride framework and Fe (II) ions to promote transfer of photogenerated electrons for selective photocatalytic reduction of Nitrophenols. *J. Colloid Interface Sci.* **2022**, *608*, 2088–2099. [[CrossRef](#)] [[PubMed](#)]
7. Najeeb, J.; Ahmad, G.; Nazir, S.; Naseem, K.; Kanwal, A. Critical analysis of various supporting mediums employed for the incapacitation of silver nanomaterial for aniline and phenolic pollutants: A review. *Korean J. Chem. Eng.* **2021**, *38*, 248–263. [[CrossRef](#)]
8. Zdarta, J.; Meyer, A.S.; Jesionowski, T.; Pinelo, M. Multi-faceted strategy based on enzyme immobilization with reactant adsorption and membrane technology for biocatalytic removal of pollutants: A critical review. *Biotechnol. Adv.* **2019**, *37*, 107401. [[CrossRef](#)]
9. Lofrano, G.; Meric, S.; Zengin, G.E.; Orhon, D. Chemical and biological treatment technologies for leather tannery chemicals and wastewaters: A review. *Sci. Total Environ.* **2013**, *461*, 265–281. [[CrossRef](#)]
10. Min, X.; Chu, C.; Luo, Z.; Ma, J.; Fu, Y.; Wei, Z.; Spinney, R.; Dionysiou, D.D.; Xiao, R. Transformation of phenol and nitrobenzene by superoxide radicals: Kinetics and mechanisms. *Chem. Eng. J.* **2022**, *442*, 136134. [[CrossRef](#)]
11. Begum, R.; Rehan, R.; Farooqi, Z.H.; Butt, Z.; Ashraf, S. Physical chemistry of catalytic reduction of nitroarenes using various nanocatalytic systems: Past, present, and future. *J. Nanopart. Res.* **2016**, *18*, 231. [[CrossRef](#)]

12. Shesterkina, A.A.; Shuvalova, E.V.; Kirichenko, O.A.; Strelkova, A.A.; Nissenbaum, V.D.; Kapustin, G.I.; Kustov, L.M. Application of Silica-supported Fe-Cu Nanoparticles in the Selective Hydrogenation of p-Dinitrobenzene to p-Phenylenediamine. *Russ. J. Phys. Chem. A* **2017**, *91*, 201–204. [[CrossRef](#)]
13. Shuvalova, E.V.; Kirichenko, O.A. Hydrogenation of nitroarenes on silica-supported copper catalyst. *Mendeleev Commun.* **2021**, *31*, 875–877. [[CrossRef](#)]
14. Zaarour, M.; Cazemier, J.; Miguel, J.C.N.d.; Almukhtar, F.; Komaty, S.; Martinez, J.R. Influence of support polarity on the selective hydrogenation of nitrostyrene over Pt-based heterogenous catalysts. *Microporous Mesoporous Mater.* **2024**, *379*, 113272. [[CrossRef](#)]
15. Park, J.; Bae, S. Highly efficient and magnetically recyclable Pd catalyst supported by iron-rich fly ash@fly ash-derived SiO₂ for reduction of p-nitrophenol. *J. Hazard. Mater.* **2019**, *371*, 72–82. [[CrossRef](#)]
16. Zheng, F.; Cao, S.; Yang, Z.; Sun, Y.; Shen, Z.; Wang, Y.; Pang, H. Synthesis and Catalytic Application of MOF Complexes Containing Noble Metals. *Energy Fuels* **2024**, *38*, 11494–11520. [[CrossRef](#)]
17. Nasrollahzadeh, M.; Sajjadi, M.; Shokouhimehr, M.; Varma, R.S. Recent developments in palladium (nano)catalysts supported on polymers for selective and sustainable oxidation processes. *Coord. Chem. Rev.* **2019**, *397*, 54–75. [[CrossRef](#)]
18. Wang, Y.-C.; Lai, Y.-R.; Wu, J.W.; Wang, S.S.S.; Lin, K.-S. Using palladium nanoparticle-decorated lysozyme amyloid fibrils to catalyze the reduction of methylene blue. *J. Taiwan Inst. Chem. Eng.* **2021**, *118*, 187–195. [[CrossRef](#)]
19. Yang, Y.; Miao, C.; Wang, R.; Zhang, R.; Li, X.; Wang, J.; Wang, X.; Yao, J. Advances in morphology-controlled alumina and its supported Pd catalysts: Synthesis and applications. *Chem. Soc. Rev.* **2024**, *53*, 5014–5053. [[CrossRef](#)]
20. Liu, J.; Luo, Z.; Li, J.; Yu, X.; Llorca, J.; Nasiou, D.; Arbiol, J.; Meyns, M.; Cabot, A. Graphene-supported palladium phosphide PdP₂ nanocrystals for ethanol electrooxidation. *Appl. Catal. B-Environ.* **2019**, *242*, 258–266. [[CrossRef](#)]
21. Diaz-Sanchez, M.; Diaz-Garcia, D.; Prashar, S.; Gomez-Ruiz, S. Palladium nanoparticles supported on silica, alumina or titania: Greener alternatives for Suzuki-Miyaura and other C-C coupling reactions. *Environ. Chem. Lett.* **2019**, *17*, 1585–1602. [[CrossRef](#)]
22. Li, J.; Fan, K.; Shan, Y.; Wang, S.; Zhang, J.; Fan, W.; He, H.; Zhao, X.; Meng, X.; Xiao, F.-S. Superior performance in passive NO_x adsorption over an Al-rich Beta zeolite supported palladium. *Appl. Catal. B-Environ. Energy* **2023**, *339*, 123127. [[CrossRef](#)]
23. Yan, B.; Zhang, L.; Tang, Z.; Al-Mamun, M.; Zhao, H.; Su, X. Palladium-decorated hierarchical titania constructed from the metal-organic frameworks NH₂-MIL-125(Ti) as a robust photocatalyst for hydrogen evolution. *Appl. Catal. B-Environ.* **2017**, *218*, 743–750. [[CrossRef](#)]
24. Deng, X.; Zhu, L.; Zhang, H.; Li, L.; Zhao, N.; Wang, J.; Osman, S.M.; Luque, R.; Chen, B.H. Highly efficient and stable catalysts-covalent organic framework-supported palladium particles for 4-nitrophenol catalytic hydrogenation. *Environ. Res.* **2022**, *214*, 114027. [[CrossRef](#)]
25. Chen, Y.; Chen, R.; Chang, X.; Yan, J.; Gu, Y.; Xi, S.; Sun, P.; Dong, X. Degradation of Sodium Acetate by Catalytic Ozonation Coupled with a Mn-Functionalized Fly Ash: Reaction Parameters and Mechanism. *Toxics* **2023**, *11*, 700. [[CrossRef](#)] [[PubMed](#)]
26. Angaru, G.K.R.; Choi, Y.-L.; Lingamdinne, L.P.; Choi, J.-S.; Kim, D.-S.; Koduru, J.R.; Yang, J.-K.; Chang, Y.-Y. Facile synthesis of economical feasible fly ash-based zeolite-supported nano zerovalent iron and nickel bimetallic composite for the potential removal of heavy metals from industrial effluents. *Chemosphere* **2021**, *267*, 128889. [[CrossRef](#)] [[PubMed](#)]
27. Gao, K.; Iliuta, M.C. Trends and advances in the development of coal fly ash-based materials for application in hydrogen-rich gas production: A review. *J. Energy Chem.* **2022**, *73*, 485–512. [[CrossRef](#)]
28. Cai, Z.; Du, B.; Dai, X.; Wang, T.; Wang, J.; Zhang, Y. Coupling of alkaline and mechanical modified fly ash for HCl and SO₂ removal in the municipal solid waste incineration plant. *Fuel* **2023**, *346*, 128354. [[CrossRef](#)]
29. Lin, J.X.; Zhan, S.L.; Fang, M.H.; Qian, X.Q.; Yang, H. Adsorption of basic dye from aqueous solution onto fly ash. *J. Environ. Manag.* **2008**, *87*, 193–200. [[CrossRef](#)]
30. Kobayashi, Y.; Ogata, F.; Nakamura, T.; Kawasaki, N. Synthesis of novel zeolites produced from fly ash by hydrothermal treatment in alkaline solution and its evaluation as an adsorbent for heavy metal removal. *J. Environ. Chem. Eng.* **2020**, *8*, 103687. [[CrossRef](#)]
31. Singh, N.B.; Agarwal, A.; De, A.; Singh, P. Coal fly ash: An emerging material for water remediation. *Int. J. Coal Sci. Technol.* **2022**, *9*, 44. [[CrossRef](#)]
32. Wang, W.; Qi, L.; Zhang, J. Specific resistance and adsorption performance of acid-modified fly ash for escaped ammonia in flue gas. *J. Hazard. Mater.* **2024**, *465*, 133072. [[CrossRef](#)]
33. Maity, N.; Mishra, A.; Barman, S.; Padhi, S.K.; Panda, B.B.; Jaseer, E.A.; Javid, M. Tuning Pd-to-Ag Ratio to Enhance the Synergistic Activity of Fly Ash-Supported PdAg Bimetallic Nanoparticles. *Acs Omega* **2023**, *9*, 1020–1028. [[CrossRef](#)]
34. Iqbal, A.; Sattar, H.; Haider, R.; Munir, S. Synthesis and characterization of pure phase zeolite 4A from coal fly ash. *J. Clean. Prod.* **2019**, *219*, 258–267. [[CrossRef](#)]
35. Yu, W.; Wu, X.; Mi, R.; Zai, H.; Fang, M.; Min, X.; Liu, Y.; Huang, Z. Synthesis of ZSM-5 zeolite from fly ash by one-pot hydrothermal method for methylene blue removal. *J. Am. Ceram. Soc.* **2024**, *107*, 5298–5312. [[CrossRef](#)]
36. Ren, X.; Xiao, L.; Qu, R.; Liu, S.; Ye, D.; Song, H.; Wu, W.; Zheng, C.; Wu, X.; Gao, X. Synthesis and characterization of a single phase zeolite A using coal fly ash. *Rsc Adv.* **2018**, *8*, 42200–42209. [[CrossRef](#)]
37. Kim, M.; Bae, S. Immobilization and characterization of Fe(0) catalyst on NaOH-treated coal fly ash for catalytic reduction of p-nitrophenol. *Chemosphere* **2018**, *212*, 1020–1029. [[CrossRef](#)] [[PubMed](#)]
38. Gao, K.; Sahraei, O.A.; Iliuta, M.C. Ni-based catalysts supported on acid/alkali-activated coal fly ash residue for improved glycerol steam reforming. *Appl. Catal. B-Environ.* **2022**, *301*, 120791. [[CrossRef](#)]
39. Zhang, P.; Yu, W.; Gao, B.; Cui, S.; Li, J.; Qi, L. Denitration performance and mechanism of Mn-Ce supported alkali-modified fly ash catalysts for NH₃-SCR. *Fuel* **2024**, *357*, 129878. [[CrossRef](#)]

40. Niveditha, S.V.; Gandhimathi, R. Flyash augmented Fe₃O₄ as a heterogeneous catalyst for degradation of stabilized landfill leachate in Fenton process. *Chemosphere* **2020**, *242*, 125189. [[CrossRef](#)]
41. Singh, G.V.P.B.; Subramanian, K.V.L. Quantitative XRD study of amorphous phase in alkali activated low calcium siliceous fly ash. *Constr. Build. Mater.* **2016**, *124*, 139–147. [[CrossRef](#)]
42. Chen, Y.; Chen, R.; Chang, X.; Yan, J.; Gu, Y.; Xi, S.; Sun, P.; Dong, X. Ozone Catalysis Degradation of Sodium Acetate via Vacancy-Driven Radical Oxidation over Fe-Modified Fly Ash. *Water* **2023**, *15*, 3801. [[CrossRef](#)]
43. Topuz, F.; Uyar, T. RNA-mediated, green synthesis of palladium nanodendrites for catalytic reduction of nitroarenes. *J. Colloid Interface Sci.* **2019**, *544*, 206–216. [[CrossRef](#)] [[PubMed](#)]
44. Li, X.; Dong, F.; Zhang, L.; Xu, Q.; Zhu, X.; Liang, S.; Hu, L.; Xie, H. Cellulosic protic ionic liquids hydrogel: A green and efficient catalyst carrier for Pd nanoparticles in reduction of 4-nitrophenol in water. *Chem. Eng. J.* **2019**, *372*, 516–525. [[CrossRef](#)]
45. Manivannan, S.; An, S.; Jeong, J.; Viji, M.; Kim, K. Hematite/M (M = Au, Pd) Catalysts Derived from a Double-Hollow Prussian Blue Microstructure: Simultaneous Catalytic Reduction of o and p-Nitrophenols. *ACS Appl. Mater. Interfaces* **2020**, *12*, 17557–17570. [[CrossRef](#)]
46. Xu, L.; Chen, D.; Qu, J.; Wang, L.; Tang, J.; Liu, H.; Yang, J. Replacement reaction-based synthesis of supported palladium catalysts with atomic dispersion for catalytic removal of benzene. *J. Mater. Chem. A* **2018**, *6*, 17032–17039. [[CrossRef](#)]
47. Chang, Q.; Xu, W.; Li, N.; Xue, C.; Wang, Y.; Li, Y.; Wang, H.; Yang, J.; Hu, S. Dynamic restructuring of carbon dots/copper oxide supported on mesoporous hydroxyapatite brings exceptional catalytic activity in the reduction of 4-nitrophenol. *Appl. Catal. B-Environ.* **2020**, *263*, 118299. [[CrossRef](#)]
48. Aslam, S.; Subhan, F.; Yan, Z.; Yaseen, M.; Shujahat, M.H. Fabrication of gold nanoparticles within hierarchically ZSM-5-based micro-/mesostructures (MMZ) with enhanced stability for catalytic reduction of p-nitrophenol and methylene blue. *Sep. Purif. Technol.* **2021**, *254*, 117645. [[CrossRef](#)]
49. Xu, Y.; Shi, X.; Hua, R.; Zhang, R.; Yao, Y.; Zhao, B.; Liu, T.; Zheng, J.; Lu, G. Remarkably catalytic activity in reduction of 4-nitrophenol and methylene blue by Fe₃O₄@COF supported noble metal nanoparticles. *Appl. Catal. B-Environ.* **2020**, *260*, 118142. [[CrossRef](#)]
50. Qian, H.; He, Q.; Zheng, J.; Li, S.; Zhang, S. Catechol-functionalized microporous organic polymer as supported media for Pd nanoparticles and its high catalytic activity. *Polymer* **2014**, *55*, 550–555. [[CrossRef](#)]
51. Ho, T.G.-T.; Truong, D.P.T.; Nguyen, H.B.; Do, B.L.; Dinh, T.A.; Ton-That, P.; Nguyen, T.T.V.; Truong, T.B.T.; Huynh, K.P.H.; Tri, N. Green synthesized nano-silver/cellulose aerogel as a robust active and recyclable catalyst towards nitrophenol hydrogenation. *Chem. Eng. J.* **2023**, *471*, 144604.
52. Maslamani, N.; Khan, S.B.; Danish, E.Y.; Bakhsh, E.M.; Akhtar, K.; Asiri, A.M. Metal nanoparticles supported chitosan coated carboxymethyl cellulose beads as a catalyst for the selective removal of 4-nitrophenol. *Chemosphere* **2022**, *291*, 133010. [[CrossRef](#)]
53. Kokate, M.; Garadkar, K.; Gole, A. Zinc-oxide-silica-silver nanocomposite: Unique one-pot synthesis and enhanced catalytic and anti-bacterial performance. *J. Colloid Interface Sci.* **2016**, *483*, 249–260. [[CrossRef](#)] [[PubMed](#)]
54. Maity, N.; Sahoo, A.; Boddhula, R.; Chatterjee, S.; Patra, S.; Panda, B.B. Fly ash supported Pd-Ag bimetallic nanoparticles exhibiting a synergistic catalytic effect for the reduction of nitrophenol. *Dalton Trans.* **2020**, *49*, 11019–11026. [[CrossRef](#)]
55. Thanh Binh, N.; Huang, C.P.; Doong, R.-A. Enhanced catalytic reduction of nitrophenols by sodium borohydride over highly recyclable Au@graphitic carbon nitride nanocomposites. *Appl. Catal. B-Environ.* **2019**, *240*, 337–347.
56. Li, Y.; Zheng, S.; Hou, S.; Chen, T.; Bai, Y.; Zhang, M.; Zhou, D.; Yang, S.; Xu, H.; Zhang, G. Construction of continuous flow catalytic reactor-HPLC system with ultrahigh catalytic activity using 2D nanoflower MOF-derived Cu₂O/Cu/PDA/CF catalyst. *J. Hazard. Mater.* **2023**, *460*, 132376. [[CrossRef](#)] [[PubMed](#)]
57. Najdovski, I.; Selvakannan, P.; Bhargava, S.K.; O'Mullane, A.P. Formation of nanostructured porous Cu-Au surfaces: The influence of cationic sites on (electro)-catalysis. *Nanoscale* **2012**, *4*, 6298–6306. [[CrossRef](#)]
58. Shokry, R.; Abd El Salam, H.M.; Aman, D.; Mikhail, S.; Zaki, T.; El Rouby, W.M.A.; Farghali, A.A.; Al, W.; Ko, Y.G. MOF-derived core-shell MnO@Cu/C as high-efficiency catalyst for reduction of nitroarenes. *Chem. Eng. J.* **2023**, *459*, 141554. [[CrossRef](#)]
59. Hunge, Y.M.; Yadav, A.A.; Kang, S.-W.; Kim, H.; Fujishima, A.; Terashima, C. Nanoflakes-like nickel cobaltite as active electrode material for 4-nitro-phenol reduction and supercapacitor applications. *J. Hazard. Mater.* **2021**, *419*, 126453. [[CrossRef](#)]
60. Chen, C.-S.; Chen, T.-C.; Chiu, K.-L.; Wu, H.-C.; Pao, C.-W.; Chen, C.-L.; Hsu, H.-C.; Kao, H.-M. Silver particles deposited onto magnetic carbon nanofibers as highly active catalysts for 4-nitrophenol reduction. *Appl. Catal. B-Environ.* **2022**, *315*, 121596. [[CrossRef](#)]
61. Xie, Z.-T.; Asoh, T.-A.; Uyama, H. Superfast flow reactor derived from the used cigarette filter for the degradation of pollutants in water. *J. Hazard. Mater.* **2020**, *400*, 123303. [[CrossRef](#)] [[PubMed](#)]
62. Sun, P.; Zhai, S.; Chen, J.; Yuan, J.; Wu, Z.; Weng, X. Development of a multi-active center catalyst in mediating the catalytic destruction of chloroaromatic pollutants: A combined experimental and theoretical study. *Appl. Catal. B-Environ.* **2020**, *272*, 119015. [[CrossRef](#)]
63. Arzac, G.M.; Montes, O.; Fernandez, A. Microstructure and activity of Pd catalysts prepared on commercial carbon support for the liquid phase decomposition of formic acid. *Int. J. Hydrogen Energy* **2023**, *48*, 2628–2639. [[CrossRef](#)]

Disclaimer/Publisher's Note: The statements, opinions and data contained in all publications are solely those of the individual author(s) and contributor(s) and not of MDPI and/or the editor(s). MDPI and/or the editor(s) disclaim responsibility for any injury to people or property resulting from any ideas, methods, instructions or products referred to in the content.